The Astrophysical Journal, 1003:204 (13pp), 2026 June 1 https://doi.org/10.3847/1538-4357/ae67fb

Detection of an Optical Quasiperiodic Oscillation in the Blazar 3C 454.3

Karan Dogra[1,2], Alok C. Gupta[1,3,4], C. M. Raiteri[5], M. Villata[5], Paul J. Wiita[6], Mauri J. Valtonen[7,8], S. O. Kurtanidze[4], S. G. Jorstad[9,10], R. Bachev[11], G. Damljanovic[12], C. Lorey[13], S. S. Savchenko[10,14,15], O. Vince[12], M. Abdelkareem[16], F. J. Aceituno[17], J. A. Acosta-Pulido[18,19], I. Agudo[17], G. Andreuzzi[20], S. A. Ata[16], G. V. Baida[21], L. Barbieri[22], D. A. Blinov[23,24], G Bonnoli[17,25], G. A. Borman[21], M. I. Carnerero[5], D. Carosati[20,26], V. Casanova[17], W. P. Chen[27], Lang Cui[3], P. U. Devanand[1,2], E. G. Elhosseiny[16], D. Elsaesser[13,28], J. Escudero[17,29], J. H. Fan[30,31,32], M. Feige[13], K. Gazeas[33], T. S. Grishina[10], Minfeng Gu[34], V. A. Hagen-Thorn[10], F. Hemrich[13], H. Y. Hsiao[27], M. Ismail[16], R. Z. Ivanidze[4], M. D. Jovanovic[12], T. M. Kamel[16], G. N. Kimeridze[4], Shubham Kishore[1,35], E. N. Kopatskaya[10], D. Kuberek[13], O. M. Kurtanidze[4,36,37], A. Kurtenkov[11], V. M. Larionov[10], Elena G. Larionova[10], L. V. Larionova[10], H. C. Lin[27], A. Marchini[38], C. Marinelli[39], A. P. Marscher[9], D. Morcuende[17], D. A. Morozova[10], S. V. Nazarov[21], M. G. Nikolashvili[4], D. Reinhart[13], J. Otero-Santos[17], A. Scherbantin[13], E. Semkov[11], E. V. Shishkina[10], L. A. Sigua[4], A. K. Singh[2], A. Sota[17], R. Steineke[13], M. Stojanovic[12], A. Strigachev[11], A. Takey[16], Amira A. Tawfeek[16], Tushar Tripathi[1], I. S. Troitskiy[10], Y. V. Troitskaya[10], An-Li Tsai[27,40], A. A. Vasilyev[10], K. Vrontaki[33], Zhongli Zhang[34,41], A. V. Zhovtan[42], N. Zottmann[13], and Wenwen Zuo[34]

[1] Aryabhatta Research Institute of Observational Sciences (ARIES), Manora Peak, Nainital 263001, India; karandogra987@gmail.com, acgupta30@gmail.com
[2] Department of Applied Physics, Mahatma Jyotiba Phule Rohilkhand University, Bareilly 243006, India
[3] Xinjiang Astronomical Observatory, Chinese Academy of Sciences, 150 Science-1 Street, Urumqi 830011, People's Republic of China
[4] Abastumani Observatory, Mount Kanobili, 0301 Abastumani, Georgia
[5] INAF, Osservatorio Astrofisico di Torino, Via Osservatorio 20, I-10025 Pino Torinese, Italy
[6] Department of Physics, The College of New Jersey, PO Box 7718, Ewing, NJ 08628, USA
[7] FINCA, University of Turku, FI-20014 Turku, Finland
[8] Tuorla Observatory, Department of Physics and Astronomy, University of Turku, FI-20014 Turku, Finland
[9] Institute for Astrophysical Research, Boston University, 725 Commonwealth Avenue, Boston, MA 02215, USA
[10] Astronomical Institute, Saint Petersburg State University, 7/9 Universitetskaya Baberezhnaya, St. Petersburg 199034, Russia
[11] Institute of Astronomy and National Astronomical Observatory, Bulgarian Academy of Sciences, 72 Tsarigradsko Shosse Boulevard, 1784 Sofia, Bulgaria
[12] Astronomical Observatory, Volgina 7, 11060 Belgrade, Serbia
[13] Hans-Haffner-Sternwarte, Naturwissenschaftliches Labor für Schüler am FKG, Friedrich-Koenig-Gymnasium, D-97082 Würzburg, Germany
[14] Special Astrophysical Observatory, Russian Academy of Sciences, 369167, Nizhnii Arkhyz, Russia
[15] Pulkovo Observatory, St. Petersburg 196140, Russia
[16] National Research Institute of Astronomy and Geophysics (NRIAG), 11421 Helwan, Cairo, Egypt
[17] Instituto de Astrofísica de Andalucía, IAA-CSIC, Glorieta de la Astronomía s/n, E-18008 Granada, Spain
[18] Instituto de Astrofísica de Canarias (IAC), E-38200 La Laguna, Tenerife, Spain
[19] Universidad de La Laguna, Departamento de Astrofísica, E-38206 La Laguna, Tenerife, Spain
[20] INAF, TNG Fundación Galileo Galilei, La Palma E-38712, Spain
[21] Crimean Astrophysical Observatory of the Russian Academy of Sciences, P/O Nauchny 298409, Russia
[22] Orciatico Astronomical Observatory, Orciatico, Pisa, Italy
[23] Institute of Astrophysics, Foundation for Research and Technology—Hellas, Voutes, 70013 Heraklion, Greece
[24] Department of Physics, University of Crete, 71003 Heraklion, Greece
[25] INAF Osservatorio Astronomico di Brera, Via Emilio Bianchi 46, 23807 Merate, Italy
[26] EPT Observatories, Tijarafe, La Palma E-38780, Spain
[27] Institute of Astronomy, National Central University, Taoyuan 32001, Taiwan
[28] Astroteilchenphysik, TU Dortmund, Otto-Hahn-Straße 4A, D-44227 Dortmund, Germany
[29] Center for Astrophysics | Harvard & Smithsonian, Cambridge, MA 02138, USA
[30] Center for Astrophysics, Guangzhou University, Guangzhou 510006, People's Republic of China
[31] Astronomy Science and Technology Research Laboratory of the Department of Education of Guangdong Province, Guangzhou 510006, People's Republic of China
[32] Greater Bay Brand Center of the National Astronomical Data Center, Guangzhou 510006, People's Republic of China
[33] Section of Astrophysics, Astronomy and Mechanics, Department of Physics, National and Kapodistrian University of Athens, GR-15784 Zografos, Athens, Greece
[34] Shanghai Astronomical Observatory, Chinese Academy of Sciences, 80 Nandan Road, Shanghai 200030, People's Republic of China
[35] Indian Institute of Astrophysics (IIA), 2nd Block, Koramangala, Bangalore 560034, India
[36] Engelhardt Astronomical Observatory, Kazan Federal University, Tatarstan, Russia
[37] Landessternwarte, Zentrum für Astronomie der Universität Heidelberg, Königstuhl 12, 69117 Heidelberg, Germany
[38] University of Siena, Astronomical Observatory, Via Roma 56, 53100 Siena, Italy
[39] Dipartimento di Scienze Fisiche, della Terra e dell'Ambiente, Universitá di Siena, Via Roma 56, 53100 Siena, Italy
[40] Department of Physics, National Sun Yat-sen University, Kaohsiung 80424, Taiwan
[41] Key Laboratory of Radio Astronomy and Technology, Chinese Academy of Sciences, A20 Datun Road, Chaoyang District, Beijing 100101, People's Republic of China

[42] Crimean Astrophysical Observatory of the Russian Academy of Sciences, P/O Nauchny 298409, Crimea†
Received 2025 July 23; revised 2026 April 21; accepted 2026 April 29; published 2026 May 26

Abstract

We analyzed 19 yr of *R*-band data of the blazar 3C 454.3 from the Whole Earth Blazar Telescope archive, along with new data from its members and from public archives such as those provided by the Small and Moderate Aperture Research Telescope System and the Steward Observatory projects to search for quasiperiodic oscillations (QPOs). We detected a QPO of ∼433 days using Lomb–Scargle periodogram, which lasted from MJD 54980–58450 as detected by the weighted wavelet Z-transform technique, making it one of the most persistent QPOs ever detected in the optical regime. The phase dispersion minimization technique was also performed to further validate this QPO claim. We detected this signal at a global significance of 2.53σ across all methodologies. To explain the observed QPO, we have considered both models focused on the accretion disk around a supermassive black hole (SMBH), and those based purely on jet emissions. Plausible jet-based models involve a shock moving down the jet in a helical magnetic field, whereas the SMBH models could involve Lense–Thirring-effect-induced jet precession or dual jets in a binary SMBH system. We introduce a novel approach to distinguish genuine QPOs from spurious signals arising from annual seasonal gaps, a common limitation of ground-based observations.

Unified Astronomy Thesaurus concepts: Active galactic nuclei (16); Blazars (164); Lomb-Scargle periodogram (1959); Wavelet analysis (1918); Markov Chain Monte Carlo (1889)

1. Introduction

The relativistic jets of blazars, a subgroup of active galactic nuclei (AGNs), point roughly in the direction of our line of sight (C. M. Urry & P. Padovani 1995). Blazars are divided into two subclasses: BL Lacertae objects (BL Lac objects) and flat-spectrum radio quasars (FSRQs). In composite near-infrared to UV spectra, strong emission lines are usually seen in FSRQs, while no significant emission or absorption lines are seen in BL Lac objects. Accreting black holes (BHs) with masses ranging from 10^6 to $10^{10}\,M_\odot$ are almost certainly present in AGNs, and they resemble scaled-up Galactic X-ray-producing BH binaries in many ways.

In our and neighboring galaxies, quasiperiodic oscillations (QPOs) are fairly frequent in both BHs and neutron star binaries (e.g., R. A. Remillard & J. E. McClintock 2006). However, the light curves (LCs) of AGNs are mostly nonperiodic throughout the whole electromagnetic (EM) spectrum, exhibiting stochastic changes that can be ascribed to accretion disk (AD) or jet instabilities (e.g., A. C. Gupta et al. 2018; A. Tripathi et al. 2021; A. Tripathi et al. 2024a, and references therein). Nonetheless, sporadic QPO detections in various EM bands with varying timescales have been argued for in a number of blazars (e.g., A. C. Gupta et al. 2009, 2019; P. Lachowicz et al. 2009; O. G. King et al. 2013; M. Ackermann et al. 2015; A. Sandrinelli et al. 2016, 2018; G. Bhatta 2017, 2019; J. Zhou et al. 2018; P. Peñil et al. 2020; A. Sarkar et al. 2020, 2021; A. Tripathi et al. 2021; S. G. Jorstad et al. 2022; A. Roy et al. 2022a, 2022b; S. Kishore et al. 2023, and references therein) especially within the past 2 decades or so. Additionally, possible QPOs have also been discussed for a few nonblazar AGNs (e.g., M. Gierliński et al. 2008; W. N. Alston et al. 2014, 2015; H.-W. Pan et al. 2016; A. C. Gupta et al. 2018; P. Peñil et al. 2020, and references therein)

3C 454.3 is one of the brightest and best-studied FSRQs, with $z = 0.859$ (A. Hewitt & G. Burbidge 1989). It has strong optical polarization, substantial variability throughout the EM spectrum, and nonthermal emission, which are all standard characteristics of an FSRQ (e.g., P. S. Smith et al. 1988; L. Fuhrmann et al. 2006; M. Villata et al. 2006, 2007, 2009; P. Giommi et al. 2006; C. M. Raiteri et al. 2007, 2008; A. A. Abdo et al. 2009; E. W. Bonning et al. 2009; M. Ackermann et al. 2010; S. G. Jorstad et al. 2010; S. Vercellone et al. 2010; M. Sasada et al. 2014; P. Mohan et al. 2015; A. C. Gupta et al. 2017; A. Sarkar et al. 2019; K. Dogra et al. 2025, and references therein). By using optical spectroscopy methods, the mass of the SMBH in 3C 454.3's central engine is estimated to be in the range of $(0.5\text{–}2.3) \times 10^9\,M_\odot$ (J.-H. Woo & C. M. Urry 2002; Y. Liu et al. 2006; T. Sbarrato et al. 2012; A. C. Gupta et al. 2017; K. Nalewajko et al. 2019).

3C 454.3 is among the blazars for which claims of an apparent QPO have been made, in radio, optical, and gamma-ray bands (J. H. Fan et al. 2021; A. Sarkar et al. 2021; A. Tripathi et al. 2024b). A simultaneous QPO with a 47 day period in the gamma-ray as well as optical LCs of 3C 454.3 was reported by A. Sarkar et al. (2021) by analyzing *R*-band optical photometric data taken from 2006 to 2018 with the 70 cm meniscus telescope at Abastumani Observatory, Georgia. In this work, we utilized ∼19 yr of optical *R*-band data of the FSRQ 3C 454.3 to search for QPOs. Because of its brightness and the large number of available observations conducted over an extended temporal span we focused our attention on this source. An initial inspection of the LC using a Lomb–Scargle periodogram (LSP) suggested a periodic feature, so we then conducted a detailed analysis. In another study conducted by J. H. Fan et al. (2021), the authors reported the detection of three possible periods in the range of ∼440–1100 days. However, their study was not able to fully resolve the temporal evolution of these signals. As the authors noted, the longer-period components appeared fused together in their weighted wavelet Z-transform (WWZ) analysis, which limited their ability to clearly distinguish their individual contributions. As a dense sampling of the source under study is

† While the AAS journals adhere to and respect UN resolutions regarding the designations of territories (available at http://www.un.org/press/en), it is our policy to use the affiliations provided by our authors on published articles.

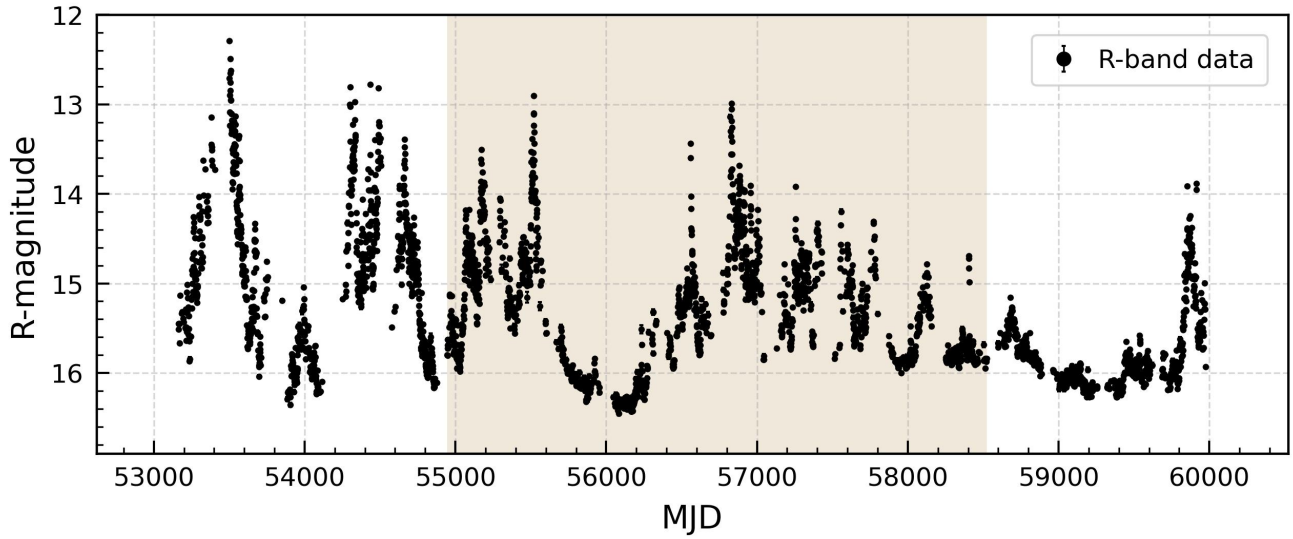

Figure 1. *R*-band LC plot of the object 3C 454.3. The plot shows the full LC from 2004 to 2023. The part of the LC where the signal is most apparent is highlighted.

Table 1
Log of Observations Obtained from the ARIES 1.3 m (A) and 1.04 m (B) Telescopes

Obs. Date (DD-MM-YYYY)	Telescope	Obs. Date (DD-MM-YYYY)	Telescope	Obs. Date (DD-MM-YYYY)	Telescope	Obs. Date (DD-MM-YYYY)	Telescope	Obs. Date (DD-MM-YYYY)	Telescope
04-11-2020	A	05-12-2020	A	10-10-2023	B	03-11-2023	B	19-11-2023	B
05-11-2020	A	25-10-2021	A	12-10-2023	B	05-11-2023	B	21-11-2023	B
06-11-2020	A	27-10-2021	A	13-10-2023	B	08-11-2023	B	09-12-2023	B
26-11-2020	A	15-12-2021	A	15-10-2023	B	14-11-2023	B	11-12-2023	B
27-11-2020	A	08-10-2023	B	17-10-2023	B	17-11-2023	B	12-12-2023	B
04-12-2020	A	09-10-2023	B	18-10-2023	B	18-11-2023	B	...	...

now available with a longer baseline, we have reanalyzed the LC to extract its frequency and temporal information with appropriate statistical methodologies discussed in the upcoming sections, given the red-noise behavior of the blazar LCs.

In simultaneous observations taken from 1979 to 2013 in five radio frequencies ranging from 4.8 to 37 GHz, a period of ∼2000 days in all frequencies was recently reported (A. Tripathi et al. 2024b). Here, using the optical *R*-band photometric data taken from 2004 to 2023 and detailed photometric results reported in K. Dogra et al. (2025) along with some additional new data taken from two optical telescopes in India, we detected a QPO in 3C 454.3 at a period of ∼433 days. We explained this QPO by a number of models based on, e.g., binary SMBH systems (e.g., M. Valtonen et al. 2008; C. Villforth et al. 2010; M. Ackermann et al. 2015), jet-based models, and Lense–Thirring (LT) precession of ADs (e.g., L. Stella & M. Vietri 1998; G. E. Romero et al. 2000; F. M. Rieger 2004; M. Liska et al. 2018).

In Section 2, we briefly describe the extensive dataset, most of which was discussed in detail in K. Dogra et al. (2025). We describe the the techniques we employed for the analysis in Section 3, while Section 4 provides a discussion and our conclusions.

2. Data Acquisition

In this work, we have used *R*-band data collected over a period of ∼19 yr (2004–2023). The majority of the data have been provided by the Whole Earth Blazar Telescope (WEBT) archive and its collaborators, and includes both published and unpublished data. Apart from that, data from public archives like the Small and Medium Aperture Research Telescope System (SMARTS) and the Steward Observatory have also been used. Details about the telescope facilities utilized can be found in Table 1 of K. Dogra et al. (2025), where the data reduction is also discussed. We have also included data from two other optical telescopes, 1.30 m and 1.04 m (telescopes A and B from here on, respectively), at the Aryabhatta Research Institute of Observational Sciences (ARIES), India. The total *R*-band LC is presented in Figure 1 with a data log for telescopes A and B in Table 1. The highlighted portion in Figure 1 is the span during which we find good evidence for a QPO using the techniques discussed in Section 3.

3. Data Analysis Methods and Results

We have analyzed those ∼19 yr of *R*-band optical data and found a fairly strong signal for the presence of QPO from MJD 54980–58450 using three different methods, i.e., LSP, WWZ and phase dispersion minimization (PDM). We first applied the LSP to identify a potential periodic component in the LC. After detecting a candidate period, we used two additional, independent techniques, WWZ and PDM, to corroborate the presence of the QPO. Once all three methods consistently indicated the same periodic signal, we calculated both local and global significance for the detected signal across

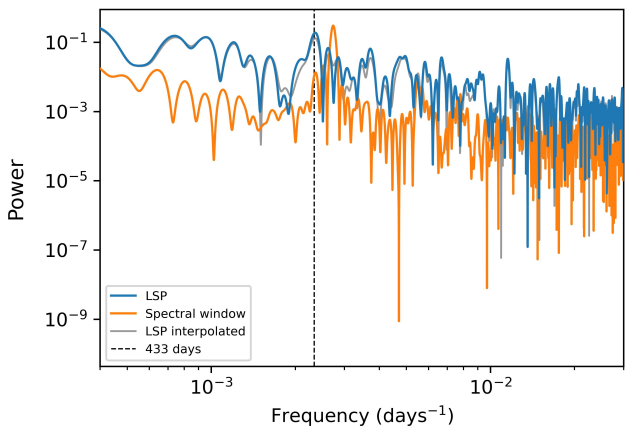

Figure 2. Plot showing the LSP of the original LC in blue, the spectral window in orange, and the LSP of the gap-interpolated original LC in gray (see Appendix).

all methodologies. Descriptions of the LSP, WWZ, and PDM methods, along with an estimation of the significance of the detected QPO, are discussed in subsections 3.1, 3.2, 3.3, and 3.4, respectively. Least squares fitting to the LC was also performed using an appropriate sinusoidal model as described in Section 3.5 to get an estimate of the error in the period of the claimed QPO and other associated parameters.

3.1. Lomb–Scargle Periodogram

LSP (N. R. Lomb 1976; J. D. Scargle 1982) is used to detect periodic signals in a data series, especially for unevenly sampled data, which makes it one of the most widely used techniques to search for periodicity. The fundamental machinery behind the LSP is just a Fourier transform, with its power p at frequency ω given by

$$p(\omega) = \frac{1}{2}\left[\frac{\left[\sum_i (m_i - \bar{m})\cos\omega(t_i - \tau)\right]^2}{\sum_i \cos^2\omega(t_i - \tau)} + \frac{\left[\sum_i (m_i - \bar{m})\sin\omega(t_i - \tau)\right]^2}{\sum_i \sin^2\omega(t_i - \tau)}\right]. \quad (1)$$

Here m_i is the ith magnitude value at time t_i, $\bar{m}$ is the average magnitude, and the parameter τ is given by

$$\tan 2\omega\tau = \frac{\sum_i \sin 2\omega t_i}{\sum_i \cos 2\omega t_i}. \quad (2)$$

In this paper, LSP has been implemented using the module `Lomb-Scargle` of the `Astropy`[43] package (Astropy Collaboration et al. 2022). The resulting LSP plot is shown in Figure 2 in blue, with the highest power corresponding to a QPO of ∼433 days.

As shown in Figure 1, several data gaps are present in the LC, most prominently the usual annual ones, which can lead to aliasing and potentially result in spurious peaks in the LSP. When applying LSP to a dataset with gaps, it is vital to take into account its failure modes, i.e., the largest peak in the LSP may not correspond to the true frequency but to some harmonic or alias of it. These effects related to the window function's structure should always be considered. Nevertheless, as mentioned in J. T. VanderPlas (2018), doing so does not guarantee that the true peak is always identified; however, it is still preferable than simply assuming that the highest peak in the periodogram is the correct one. The relevant tests and their results are as follows.

(1) *Harmonic test.* We tested whether the 433 day peak could be a harmonic of a longer true period by evaluating the Lomb–Scargle power at the harmonic frequencies $f_{\rm peak}/m$ for at least $m \in \{2, 3\}$, corresponding to ≈866 days and 1299 days. As no significant peak compared to 433 days was found at either of these periods, we conclude that the 433 day peak is not a harmonic.

(2) *Aliasing test.* To test whether the 433 day peak originated from window-function aliasing, we used the strongest window-function component at 365 days ($\delta f = 1/365$ day^{-1}) and searched for periodogram peaks at alias frequencies $|f_{\rm peak} \pm n\delta f|$ for at least $n \in \{1, 2\}$ corresponding to ≈198 days, 128 days, 315 days and, 2324 days. None of the alias candidates produced a Lomb–Scargle power greater than or equal to the 433 day peak, indicating that the 433 day QPO is not a product of aliasing.

A recent study (P. Peñil et al. 2025) demonstrated that the reliability of period detection deteriorates significantly when gaps account for more than 50% of an LC. In our case, the fraction of missing data is approximately 37%, which remains below this threshold. Therefore, the gaps in our dataset are not expected to introduce the severe degradation reported in that study. We address additional aspects of the issues arising from data gaps and possible solutions to them in the Appendix, where interpolation and its use in distinguishing actual QPOs from yearly seasonal gap artifacts using simulated LCs are discussed. We simulated LCs for spectral indices ranging from $\alpha = 1.50$–2.50, incorporating QPO periods between 250 and 500 days. We found that for more than 98% of the tested periods in the simulations, the change in QPO power before and after interpolation remains below 15% across all spectral indices. Regarding global significance (see Section 3.4), the original LC exhibited a change of less than 5%. In contrast, for simulated cases where the maximum-power change occurred, the corresponding change in global significance reaches approximately 17%. Additional details and extended results are presented in the Appendix.

The LSP method is robust and provides a good estimate of the overall power of the frequency components present, but it does not describe when, during the time series, a particular signal was present (at least for a quasiperiodic signal), and for how long it persisted. To obtain information of this type, an alternative approach is necessary, as discussed in Section 3.2.

3.2. Weighted Wavelet Z-transform

Another technique for detecting periodic signals in unevenly sampled data that is employed frequently is WWZ (e.g., G. Foster 1996). This technique not only detects periodicities but also tracks the evolution of the period, amplitude, and phase in the time series under study, which makes it a great choice when searching for QPOs. Due to its unique property of exploring both the time and frequency domains, unlike

[43] `Astropy` is a community-developed Python package that provides tools and resources for astronomy and astrophysics. It is used for a variety of tasks, including astronomical research, data processing, and data analysis.

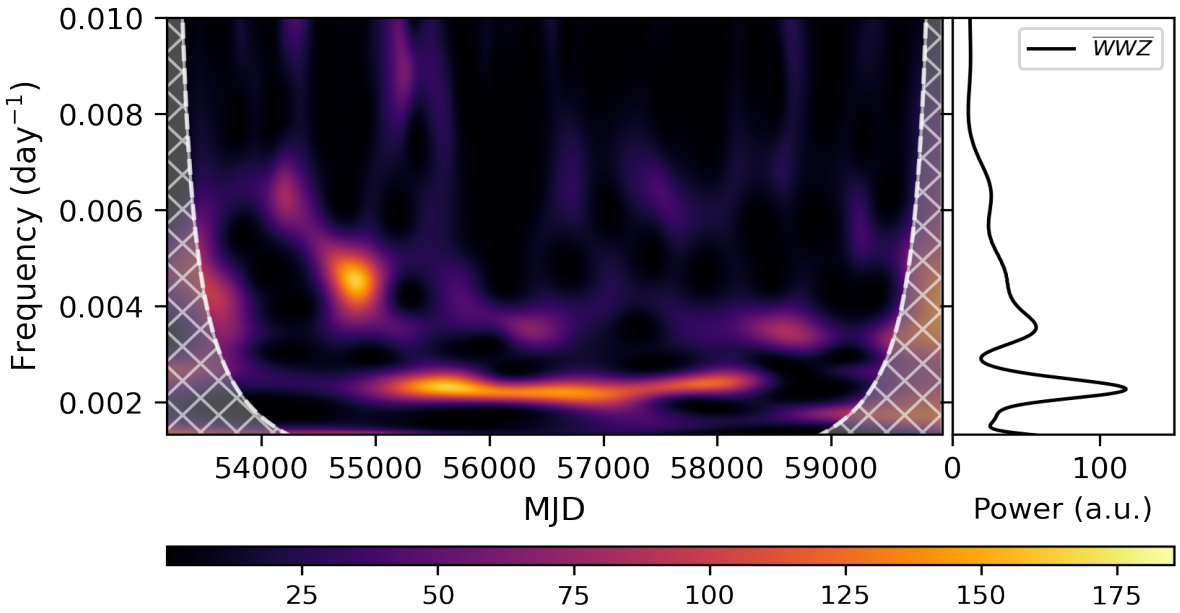

Figure 3. On left: result of the WWZ analysis with a dominant signal at 0.00231 day^{-1} from MJD 54980–58450. The white dashed line separates the region in the WWZ plot, where edge effects become dominant, with our QPO of ∼433 days in the safe region. On right: time-averaged WWZ ($\overline{WWZ}$) plot.

periodograms, it generates results as a function of both frequency and time. This yields a 3D plot with time normally shown along the x-axis, the frequency along the y-axis, and the z-axis representing the WWZ output, which is typically plotted using a color bar. The wavelet transform (WT) of a function $y(t)$ is given as

$$\begin{aligned} \mathrm{WT}(\omega, \tau; y(t)) &= \omega^{1/2} \int y(t) f^*(\omega(t-\tau))\, dt \\ &= \omega^{-1/2} \int y(\omega^{-1}z + \tau) f^*(z)\, dz. \end{aligned} \tag{3}$$

The function $f(z)$ in Equation (3) is the wavelet kernel, also known as the mother wavelet, with $f^*(z)$ being its complex conjugate. As can be seen, the WT depends on two factors: the frequency ω and the time shift τ. We have used the frequently employed Morlet wavelet, which has a Gaussian decay profile of the following mathematical form:

$$\begin{aligned} f(z) &= e^{-cz^2}(e^{iz} - e^{-1/4c}), \\ &= e^{-c\omega^2(t-\tau)^2}(e^{i\omega(t-\tau)} - e^{-1/4c}). \end{aligned} \tag{4}$$

Here, the constant c controls the rate at which the chosen wavelet decays. It is set in such a way that the exponential term in Equation (4) decays significantly in one cycle. A critical reason for having the term $e^{-1/4c}$ in the above equation is to make the average value of the wavelet zero, such that

$$\int_{-\infty}^{+\infty} f(z)\, dz = 0. \tag{5}$$

Although c can be treated as a free parameter, a popular choice for this constant is $1/8\pi^2$, the value we have adopted in this analysis. That makes the second terms within the parentheses in Equation (4), i.e., $e^{-1/4c}$, negligible, and hence gives us the so-called abbreviated Morlet transform:

$$f(z) = e^{iz - cz^2}. \tag{6}$$

To perform WWZ, the Python package `wwz`[44] (S. Kiehlmann et al. 2023), based on Foster's algorithm, has been used. The resulting WWZ plot can be seen in Figure 3 with a prominent quasiperiodic signal of 0.00231 day^{-1} or ∼433 days persisting for around 3400 days with some modulation in frequency that coincides with the LSP peak at ∼433 days in Figure 2. The cross-hatched region bounded by white dashed lines demarks the cone of influence (COI). The construction of the COI in WWZ analysis is crucial when signals appear near the edges of the time domain. In such cases, edge effects can artificially stretch the signal, creating the impression that a periodic component lasts longer than it actually does. This effect is particularly exaggerated at lower frequencies, where the wavelet extends over a larger portion of the time series. Unless a sufficiently large dataset is available so that the edge effects are minimal, the COI should always be defined. Omitting it can lead to misleading conclusions about the duration of the detected periodicity. As can be seen in Figure 3, the 433 day QPO is well within the safe region.

3.3. Phase Dispersion Minimization

In order to increase one's confidence in a detected signal, another technique known as PDM (R. F. Stellingwerf 1978) can be performed, which is well suited for searching nonsinusoidal signals. An LC with N number of (t_i, m_i) sets, where m_i is the magnitude or flux at time t_i, is phase folded at a trial period and is then divided into M phase bins, with each bin having n_j data points with similar phases. The variance in

[44] https://github.com/skiehl/wwz

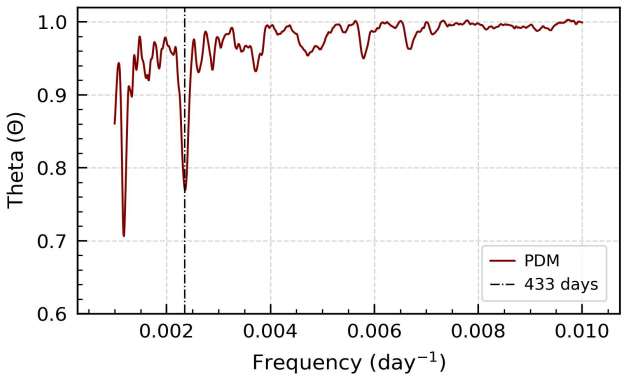

Figure 4. PDM plot and 433 day QPO dip shown by a dotted–dashed line, which is also detected in the LSP and time-averaged WWZ.

each bin is given by

$$s_j^2 = \frac{\sum_{j=1}^{M}(x_{kj} - x_j)^2}{n_j - 1}, \tag{7}$$

where x_{kj} is the kth data point in the jth phase bin. Then the net variance for all the phase bins at a particular trial period is given by

$$s^2 = \frac{\sum_{j=1}^{M}(n_j - 1)s_j^2}{\sum_{j=1}^{M} n_j - M}. \tag{8}$$

If the variance of the full LC is given by

$$\sigma^2 = \frac{\sum_{i=1}^{N}(m_i - \bar{m})^2}{N - 1}, \tag{9}$$

then the PDM statistic, θ, is the ratio of the net variance of the phase bins at a trial period to the variance of the full LC, i.e., $\theta = s^2/\sigma^2$. Thus, θ is essentially a measure of the scatter of sample variance around the mean of the LC.

To perform the PDM analysis, we used the module `PyPDM` from the `PyAstronomy`[45] (S. Czesla et al. 2019) package. For a nonsinusoidal or aperiodic variation, $s^2 \approx \sigma^2$, and θ is close to one, whereas if a periodic component is present in the LC, θ is expected to be low, so the plot will have a local minimum at that period. So, by repeating this process for a set of trial periods, one can identify any dominant period(s) in the time series. As can be seen in Figure 4, a dip is detected in the PDM plot for 3C 454.3 corresponding to a 433 day period, as detected earlier in both the LSP and WWZ analyses. Once a putative QPO signal has been detected, its significance must be estimated, as discussed in Section 3.4.

3.4. Quasiperiodic Oscillation Significance Estimation

As blazar LCs are red-noise dominated, the significance of a probable signal in LSP, WWZ, and PDM needs to be estimated. To do so, the underlying models are assumed, giving rise to the observed power spectral density (PSD) and the probability density function (PDF) of the optical LC. The best model was chosen such that Akaike's information criterion (AIC), AIC $= 2k - 2\ln(L)$, is minimized, where k is the number of free parameters and $\ln(L)$ is the log likelihood. For modeling the

[45] PyAstronomy is a collection of astronomy-related packages hosted on GitHub.

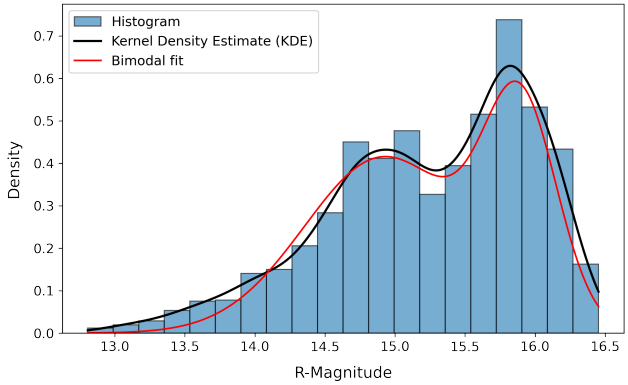

Figure 5. PDF for the R-band optical LC. To estimate the function, KDE was performed (shown in black), revealing a bimodal distribution, which was then fitted using a bimodal function (shown in red).

Table 2
Fitting Functions and Their Associated Parameters

Fitting Function	Fitting Parameters	AIC
Broken power-law function	$A = 24.223 \pm 0.943$	91,797.28
...	$f_b = 0.0024 \pm 0.0001$	...
...	$\alpha_{\rm low} = 0.553 \pm 0.013$	...
...	$\alpha_{\rm high} = 1.442 \pm 0.044$	...
Bimodal function	$A_1 = 0.516 \pm 0.022$	4582.92
...	$\mu_1 = 15.345 \pm 0.040$	...
...	$\sigma_1 = 0.736 \pm 0.038$	...
...	$A_2 = 0.641 \pm 0.166$	...
...	$\mu_2 = 15.345 \pm 0.021$	...
...	$\sigma_2 = 0.068 \pm 0.021$	...

PSD, three models, namely a power law (I. M. McHardy et al. 2004; A. A. Abdo et al. 2010; G. Bhatta & N. Dhital 2020), a broken power law (J. Otero-Santos et al. 2024), and a bending power law (S. Vaughan et al. 2016), were chosen because of the essentially red-noise behavior of the underlying PSD. Among these, the broken power law had the lowest AIC value of 91,797, while the power law and smoothly bending power law returned AIC values of 101,944 and 91,882, respectively. In analyzing the PDF we first performed an Anderson–Darling test, which rejected the null hypothesis that the PDF distribution of the LC is Gaussian at a significance level of 10^{-3}. To get an idea of the shape of the PDF we performed a kernel density estimation (KDE), which revealed a bimodal distribution as shown in Figure 5. We then made a bimodal fit to the PDF and computed its AIC, which came out to be 4583, which we compared with the AIC of the Gaussian fit, which was 4987. Thus we prefer the bimodal function. The fitting functions and their corresponding fitting parameters and AIC values can be found in Table 2.

The final PSD and PDF model functional forms are given below in Equations (10) and (11):

$$\mathrm{PSD}(f) = \begin{cases} A\left(\dfrac{f}{f_b}\right)^{-\alpha_{\rm low}}, & \text{if } f \leqslant f_b, \\ A\left(\dfrac{f}{f_b}\right)^{-\alpha_{\rm high}}, & \text{if } f > f_b. \end{cases} \tag{10}$$

Here, A is the amplitude, f_b is the break frequency, and $\alpha_{\rm low}$ and $\alpha_{\rm high}$ are the power-law indices below and above f_b,

respectively. Next:

$$\mathrm{PDF}(m) = A_1 \exp\left(-\frac{(m-\mu_1)^2}{2\sigma_1^2}\right) + A_2 \exp\left(-\frac{(m-\mu_2)^2}{2\sigma_2^2}\right). \quad (11)$$

Here A_i, μ_i, and σ_i represent the amplitude, mean, and standard deviation of a particular Gaussian, respectively.

Once the appropriate parameters for the underlying PSD and PDF were extracted, 2×10^6 LCs were simulated, with the same data sampling as for the original LC, using the EMP 13 technique (D. Emmanoulopoulos et al. 2013) implemented in the Python code `lcsim`[46] (S. Kiehlmann 2023). Unlike the TK95 algorithm (J. Timmer & M. König 1995), in which only the PSD, along with the mean and standard deviation of the original LC, are preserved in the simulated LCs, EMP 13 also preserves the PDF of the LC. Using these simulated LCs, we calculated the global significance of the detected period, which incorporates the effect of the presence of such a dominant signal at other frequencies, as opposed to the local significance (also called the single period p-value) found only at a target frequency. To evaluate the global significance, we accounted for the "look-elsewhere" effect by estimating the probability of obtaining apparently significant peaks purely from noise when scanning across a broad frequency range as described in S. O'Neill et al. (2022). To do so, we first calculated the p-value corresponding to the 433 day QPO peak, p_{qpo}, which corresponds to the local significance, by finding the number of simulations that resulted in a peak at 433 days with equal or more power, and then dividing this number by the total number of simulations. We found a local p-value of 4.71×10^{-6}, corresponding to a local significance of 4.43σ. Then we find the LSP for each simulation, and the strongest peak and its corresponding period are noted. Next, following the above procedure for the local p-value, we compute p_{sim}. Finally, we count all the simulations whose $p_{\mathrm{sim}} \leqslant p_{\mathrm{qpo}}$ and divide this number by the total number of simulations to get the global p-value and the corresponding significance. We found a global p-value of 1.87×10^{-3} corresponding to a global significance of 2.90σ.

We also calculated the global p-values for the WWZ and PDM methods, which were similar to, but greater than, the global p-value for the LSP approach: 2.21×10^{-3} (WWZ) and 2.21×10^{-3} (PDM). As we have employed three different techniques, among which the LSP returned the smallest global p-value (i.e., the highest significance), we now apply the Bonferroni correction (H. Abdi et al. 2007) to obtain a single global p-value across all methodologies. This correction is applied when multiple independent tests are performed on a dataset, thereby increasing the chance of at least one false positive. Though more conservative, the Bonferroni correction addresses this by tightening the threshold. If n represents the number of tests performed and p represents the smallest p-value among the tests, then the corrected global p-value is given by $n \times p$. We found that the global p-value across all methods is 5.61×10^{-3}, corresponding to 2.53σ.

3.5. Least Squares Fitting of the Light Curve

We fitted a sinusoidal model to the LC of the form

$$y_{\mathrm{model}}(t) = A \sin(2\pi f (t_i - t_0) - \phi_0) + y_0. \quad (12)$$

Here, A is the amplitude, $t_0 = 57{,}000$ (midpoint of the LC), $P = 1/f$ is the period, ϕ_0 is the phase of the sinusoid, and y_0 is the mean of the LC. To find the best parameters, we maximized the following likelihood:

$$\ln(L) = -\frac{1}{2}\sum_i^N \left(\frac{(y_i - y_{\mathrm{model}})^2}{\sigma_i^2 + \sigma_0^2} + \ln(\sigma_i^2 + \sigma_0^2)\right), \quad (13)$$

where y_i, σ_i, and σ_0 are the LC data points, observational errors, and Gaussian white noise, respectively. Using maximum likelihood estimate (MLE), we found the best-fitting parameters. As the MLE does not directly provide parameter errors, we used the `emcee`[47] (D. Foreman-Mackey et al. 2013) package to perform Markov Chain Monte Carlo (MCMC) sampling, initialized with the MLE-derived estimates. We reported uncertainties as the 68% confidence intervals derived from the marginalized posterior distribution, as shown in Figure 6. We found that a period of ≈433 days fits the LC well. A general practice is to fit the LSP peak to quote the error in period or frequency, but that would not be a correct approach, as the number of data points and signal-to-noise ratio do not affect the peak width but only the peak height, as explained in Section 7.4 of J. T. VanderPlas (2018), which makes the MCMC fitting a better approach.

4. Discussion and Conclusions

This project involved data from several telescopes worldwide in collaboration with the WEBT team. We employed the LSP, the WWZ, and the PSD methods to search for QPOs. We have detected a signal in the LC segment highlighted in Figure 1 from MJD 54980–58450 that has a period of ∼433 days. This corresponds to ≈8 cycles, as can be seen in Figure 3. This signal is detected at a global significance of 2.53σ. J. H. Fan et al. (2021) reported the possible presence of QPOs with data spanning from 2006 to 2018. In our reanalysis of the LC, we identify only a 433 day periodicity in the LC. The difference in results can arise because our dataset contains a larger number of observations with 12,096 data points (compared to 8523 points in the study mentioned above) over the same interval, and also spans a longer temporal baseline. These improvements reduce edge effects and enhance the reliability of signal detection. Our results indicate that a 433 day signal is consistently present from 2009 to 2018, and its statistical significance has been rigorously assessed using the methods described in this work.

QPOs in blazars are generally interpreted within three broad frameworks: models based on jet dynamics, those linked to processes around the central supermassive BH (SMBH), and scenarios involving binary SMBH systems. As the object under study is a blazar, with its jet pointing close to the line of sight of the observer, the jet emission is Doppler boosted; hence, any variability and, in turn, any QPOs detected, probably can be explained using jet emission models. P. A. Hughes et al. (1985) proposed shocks as the main driving component behind the outbursts observed in BL Lac

[46] https://github.com/skiehl/lcsim

[47] https://emcee.readthedocs.io/en/stable/

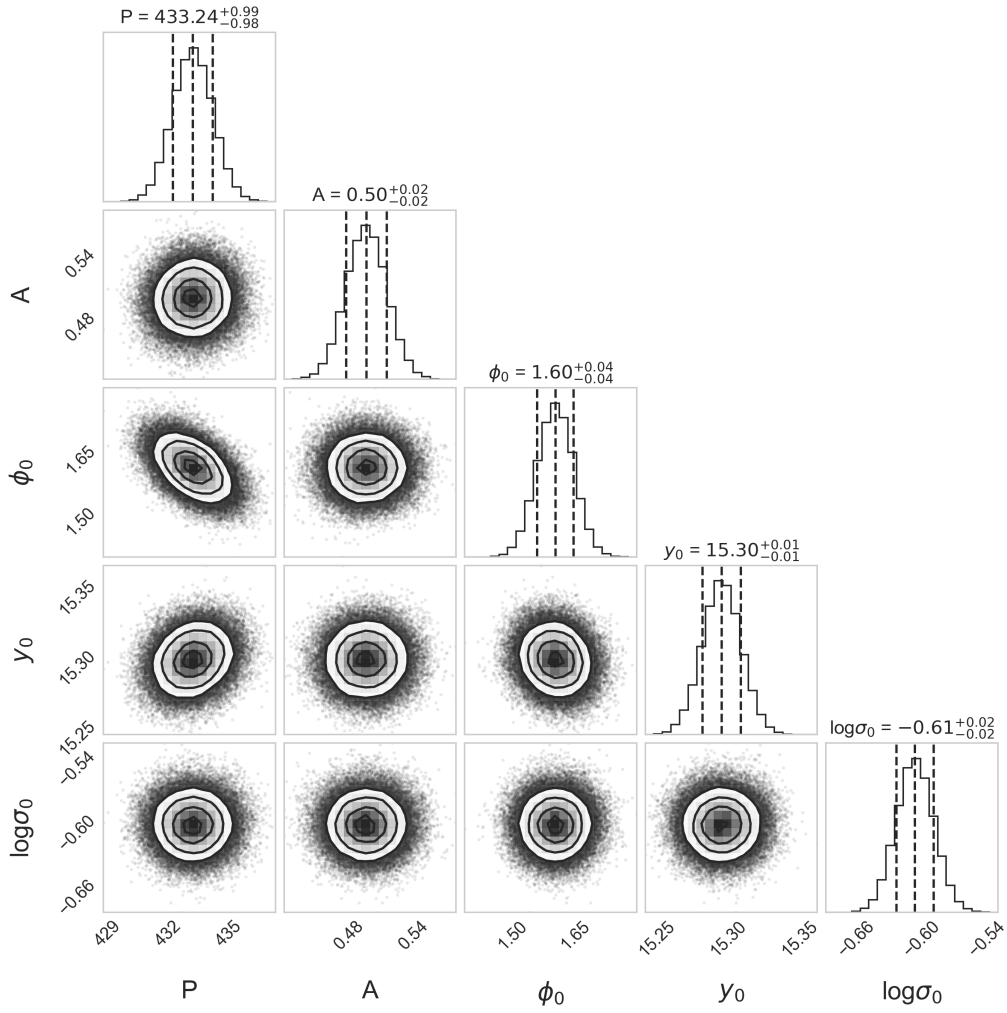

Figure 6. Corner plot showing a 2D projection of the posterior probability distribution of the sinusoidal model parameters given in Equation (12).

objects in 1982 and 1983, causing the emission to be polarized due to compression of initially random magnetic field. So, when a shock propagates down the jet in a region with a dominant helical magnetic field (e.g., A. P. Marscher et al. 2008), it can produce QPOs due to the delicate dependence of the Doppler factor on the viewing angle, $\theta(t)$, given that the shock speed changes between the helical winds (P. J. Wiita 2011), making the effect similar to a jet changing its direction. The observed flux F_ν is given by

$$F_\nu = \delta(t)^{3+\alpha} F'_{\nu'}, \tag{14}$$

where $F'_{\nu'}$ is the rest-frame flux, and the Doppler factor is $\delta(t) = 1/\Gamma(1 - \beta\cos\theta(t))$. For a blazar with optical spectral index, of say, $\alpha = 1.5$, and viewing angle in the range 1°–5°, a change in viewing angle even by 1° would cause the apparent flux to change by a factor of 2 or more (e.g., G. Bhatta & N. Dhital 2020).

Another possible way in which a QPO involving a propagating (A. P. Marscher et al. 1992) or standing (A. P. Marscher et al. 2008) shock could arise would be from the presence of a dominant cell in the strong turbulent flow behind these shocks in the jet. Because of the stochastic nature of the turbulence, the QPO would typically appear only for a limited time (e.g., P. J. Wiita 2011).

Nevertheless, emission variations produced in a binary SMBH system and in an SMBH system can provide viable explanations for such a QPO in 3C 454.3, as it is an FSRQ, having a bright AD that leaves its imprint visible in the spectral energy distribution (G. Bonnoli et al. 2011)

Another possible mechanism involves a tilted AD and LT precession (B. Mashhoon et al. 1984), occurring due to relativistic frame dragging by the central SMBH due to its spin. The precession time period ($T_{\rm LT}$) around a Kerr BH with spin parameter $a_{\rm s}$ and mass M at a distance r in the equatorial plane of the BH is given by

$$T_{\rm LT} = 0.18\left(\frac{1}{a_{\rm s}}\right)\left(\frac{M}{10^9\, M\odot}\right)\left(\frac{r}{r_g}\right)^3 \text{days}. \tag{15}$$

Considering a maximally rotating BH, this would happen around the inner part of the AD corresponding to ∼10 Schwarzschild radii (r_g), for the detected period. M. Liska et al. (2018) conducted a study using 3D general relativistic magnetohydrodynamical simulations (for different magnetic fluxes and resolutions) running for (0.3–1.2) × $10^5 t_g$. They concluded that the disk–jet system undergoes LT precession, aligning with the BH spin, with faster alignment for stronger magnetic flux strengths. This would result in jet precession,

which would, in turn, cause the Doppler factor, and hence observed brightness, to vary quasiperiodically.

Apart from jet- and AD-based models, binary SMBH systems can also produce QPOs either directly, if the secondary SMBH impinges onto the AD of the primary (e.g., H. J. Lehto & M. J. Valtonen 1996; A. C. Gupta et al. 2023), or by inducing periodic fluctuations in the accretion rate because of an elliptical orbit (e.g., G. G. Wang et al. 2022). Due to the cosmological redshift, the period in the source frame is shortened by a factor of $(1+z)$, or $\sim$233 days for a period of $\sim$433 days in the observer frame. If we consider this to be the orbital period (T) of the secondary with mass m, around a central SMBH with mass M and assuming a Keplerian orbit, the time period is given by

$$T = 1.08 \times 10^6 \left(\frac{a}{1\,\mathrm{pc}}\right)^{3/2} \left(\frac{M+m}{10^9\,M_\odot}\right)^{-1/2} \text{days}. \quad (16)$$

Taking the central SMBH mass to be $\sim 0.85 \times 10^9\,M_\odot$ (K. Nalewajko et al. 2019), we find that the binary SMBH system will have a separation, a, of order of a few milliparsecs. The gravitational-wave-driven timescale (t_{GW}) (P. C. Peters 1964) at such separations will be $\sim 10^4$–10^6 yr, assuming a mass ratio between 0.1 and 0.001 and a circular orbit.

Geometrical models can explain quasiperiodic variations without requiring a change in the intrinsic jet flow owing to the changing Doppler boosting. These models include jet precession (A. Caproni et al. 2013), a helical jet (J. E. Conway & D. W. Murphy 1993; J. Zhou et al. 2018), or a curved helical jet (C. M. Raiteri et al. 2015; A. Sarkar et al. 2021). These phenomena take place especially in binary SMBH systems, as is detailed in the models for the blazar OJ 287 (see M. J. Valtonen 2024; M. J. Valtonen et al. 2024, and references therein). In this case, the origin of each jet is in constant motion, which causes it to change direction with respect to the observer in a cyclic manner due to aberration. For equal-mass binaries in a circular orbit, the pattern is simplest: each jet may point toward us (or closest to our direction) once per orbit cycle. This may produce two equally spaced radiation peaks per orbital cycle. The peaks from the second BH's jet lie halfway between the peaks from the first jet only when the BH masses are equal and the orbit is circular; otherwise, we may have two sets of brightness peaks that are arbitrarily displaced relative to each other but still have the same periodicity, though with different amplitudes. The precession of the binary's major axis complicates this simple picture; as a result, we do not see exact periods but rather quasiperiodicity in the LC. One example of this kind is the beaming model by M. Villata et al. (1998), put forth to explain the quasiperiodicity of the double-peaked optical outbursts observed in OJ 287. Spin–orbit interaction has a qualitatively similar effect. The binary motion, therefore, produces a helical jet structure, meaning that the times of the maximum radiation peaks depend on the distance along the jet, which typically varies with the observing frequency. In the case of 3C 454.3, the 433 day quasiperiodicity appears occasionally as an exact interval between two peaks in the LC, e.g., the peak at MJD 55530 and the three peaks before and after it at this time interval. Unlike in the OJ 287 binary model, where orbital parameters are claimed to be fully determined (L. Dey et al. 2018) and lead to predictable flares, here we have too many parameters to determine all at once. Trying to do so would be an extremely interesting future study. Since the period is relatively short in comparison with that of OJ 287, one could perhaps reach the level of predictability in 3C 454.3 after a few more orbital cycles if this FSRQ indeed houses a binary SMBH system.

There have been instances in which periodicity in an SMBH system evolves, appears, or disappears, as in our case. An illustrative example is the blazar PKS 2131-021, where a periodic signal was detected in radio LCs from UMRAO, OVRO, and Haystack Observatory (S. O'Neill et al. 2022; S. Kiehlmann et al. 2025). When the data were divided into three epochs, the authors found periodicity only in the first and third epochs; sinusoidal variations were absent in epoch 2 (1983–2003). They suggest that because blazar variability is largely stochastic, sinusoidal or quasiperiodic variations may sometimes represent a special case even in binary SMBH systems. According to S. O'Neill et al. (2022), the observed variability can be interpreted as a superposition of two processes: (1) an intermittent periodic component from binary SMBH interactions and (2) stochastic jet emission from multiple regions. Variations in their relative strengths naturally lead to different observed behaviors from noisy quasiperiodic signals, from cleaner periodic modulations when the binary dominates, to more complex, nonsinusoidal structures when stochastic emission is dominant. Although a candidate case, it still provides insight into how periodic variation may appear intermittently.

However, it must be noted that A. M. Holgado et al. (2018) constructed mock blazar populations based on the luminosity functions of BL Lac objects and FSRQs with $z \leqslant 2$ to model the stochastic gravitational-wave background from SMBH binaries. Comparing their predictions to pulsar timing array limits, they found consistency only if $\sim$0.1% of blazars host a binary with an orbital period < 5 yr. A recent update using 15 yr of NANOGrav data raises this limit to $\lesssim$0.5% (S. Kiehlmann et al. 2025). Hence, we do not expect the SMBH binary explanation for the blazar QPO phenomenon to be correct very often. Apart from that, the inferred gravitational-wave-driven timescale (t_{GW}) also makes this scenario statistically less plausible.

Although the periodic signal reaches a global significance of $\approx 2.5\sigma$, we note that stochastic variability in blazar LCs can occasionally produce QPO-like features over finite time intervals. Red-noise processes are known to generate spurious peaks in periodograms with moderate statistical significance. While our simulations account for this effect, we cannot entirely exclude the possibility that the feature represents a statistical fluctuation of an underlying stochastic process. Therefore, the detected period should be interpreted conservatively.

In summary, while binary SMBH scenarios provide an appealing framework to explain QPOs in blazars, current observational constraints make them unlikely to be generally applicable. Models relying on processes within relativistic jets, conceivably initiated in the ADs around a single SMBH, offer more plausible explanations for the observed QPO signatures. Currently, the data do not permit a definitive distinction among these scenarios; however, future long-term monitoring may help establish the physical origin of the apparent QPO and determine whether it reflects a persistent dynamical mechanism or a transient manifestation of stochastic variability.

Acknowledgments

We thank the reviewer for their useful comments, which helped us improve the manuscript.

Based on data taken and assembled by the WEBT collaboration and stored in the WEBT archive at the Osservatorio Astrofisico di Torino—INAF.[48] This study was based in part on observations conducted using the 1.8 m Perkins Telescope Observatory (PTO) in Arizona, which is owned and operated by Boston University. This paper has made use of up-to-date SMARTS optical and near-infrared LCs that are available at https://www.astro.yale.edu/smarts/glast/home.php. Data from the Steward Observatory spectro-polarimetric monitoring project were used. This program is supported by Fermi Guest Investigator grants NNX08AW56G, NNX09AU10G, NNX12AO93G, and NNX15AU81G. The ZTF survey is supported by the U.S. National Science Foundation under grants no. AST-1440341 and AST-2034437. The Skinakas Observatory is a collaborative project of the University of Crete, the Foundation for Research and Technology—Hellas, and the Max-Planck-Institut für Extra-terrestrische Physik. This article is partly based on observations made with the IAC80, the STELLA, and the LCOGT 0.4 m telescopes. The IAC80 telescope is operated by the Instituto de Astrofísica de Canarias in the Spanish Observatorio del Teide on the island of Tenerife. Many thanks are due to the IAC support astronomers and telescope operators for supporting the observations at the IAC80 telescope. The STELLA robotic telescopes are an AIP facility jointly operated by AIP and IAC. One of the nodes of the LCOGT 0.4 m telescope network is located in the Spanish Observatorio del Teide. The *R*-band photometric data from the University of Athens Observatory (UOAO) were obtained after utilizing the robotic and remotely controlled instruments at the facilities.

A.C.G. is partially supported by the CAS President's International Fellowship Initiative (PIFI), grant No. 2026PVA0040. The Abastumani team acknowledges financial support by the Shota Rustaveli NSF of Georgia under contract FR-24-515. C.M.R., M.V., and M.I.C. acknowledge financial support from the INAF Fundamental Research Funding Call 2023 (PI: Raiteri). The research at Boston University was supported in part by several NASA Fermi Guest Investigator grants; the latest are 80NSSC22K1571 and 80NSSC23K1507. R.B., E.S., and A.S. were partially supported by the Bulgarian National Science Fund of the Ministry of Education and Science under grants KP-06-H68/4 (2022), KP-06-H88/4 (2024), and KP-06-KITAJ/12 (2024). G.D., O.V., M.D.J., and M.S. acknowledge support from the Astronomical station Vidojevica, funding from the Ministry of Science, Technological Development and Innovation of the Republic of Serbia (MSTDIRS; contract no. 451-03-136/2025-03/200002), by the EC through project BELISSIMA (call FP7-REGPOT-2010-5, No. 256772), the observing and financial grant support from the Institute of Astronomy and Rozhen NAO BAS through the bilateral SANU-BAN joint research project "Gaia astrometry and fast variable astronomical objects," and support by the SANU project F-187. Also, this research was supported by the Science Fund of the Republic of Serbia, grant No. 6775, Urban Observatory of Belgrade—UrbObsBel. The NRIAG team acknowledges financial support from the Egyptian Science, Technology & Innovation Funding Authority (STDF) under grant No. 45779. The *R*-band photometric data from the University of Athens Observatory (UOAO) were obtained in the frame of BOSS Project (K. Gazeas 2019) after utilizing the robotic and remotely controlled instruments at the University of Athens (K. Gazeas 2016). The IAA-CSIC coauthors acknowledge financial support from the Spanish "Ministerio de Ciencia e Innovación" (MCIN/AEI/10.13039/501100011033) through the Center of Excellence Severo Ochoa award for the Instituto de Astrofísica de Andalucía-CSIC (CEX2021-001131-S), and through grants PID2019-107847RB-C44 and PID2022-139117NB-C44. Some of the data are based on observations collected at the Observatorio de Sierra Nevada, which is owned and operated by the Instituto de Astrofísica de Andalucía (IAA-CSIC), and at the Centro Astronómico Hispano en Andalucía (CAHA), which is operated jointly by Junta de Andalucía and Consejo Superior de Investigaciones Científicas (IAA-CSIC). L.C. acknowledges the support from the Tianshan Talent Training Program (grant No. 2023TSYCCX0099). J.H. F's work is partially supported by the National Natural Science Foundation of China (NSFC 12433004 and U2031201), the Eighteenth Regular Meeting Exchange Project of the Scientific Technological Cooperation Committee between the People's Republic of China and the Republic of Bulgaria (Series No. 1802). J.H.F. also acknowledges the science research grants from the China Manned Space Project with No. CMS-CSST-2024-A07. M.F.G. is supported by the National Science Foundation of China (grant 12473019), the China Manned Space Project with No. CMS-CSST-2021-A06, the National SKA Program of China (grant No. 2022SKA0120102), and the Shanghai Pilot Program for Basic Research-Chinese Academy of Science, Shanghai Branch (JCYJ-SHFY-2021-013). Z.Z. is funded by the National Science Foundation of China (grant No. 12233005).

Facilities: ARIES Observatory, SMARTS Observatory, Steward Observatory, WEBT Collaboration (K. Dogra et al. (2025).

Software: `Astropy`, `wwz`, `PyAstronomy`, `lcsim`, `emcee`.

Appendix
Testing the Effect of the Spectral Window and Seasonal Gaps

Gaps in an LC, particularly recurring seasonal gaps caused by observing constraints, maintenance, or weather, can strongly affect periodogram analyses by introducing aliasing features. A standard diagnostic for assessing such effects is the spectral window, constructed by replacing the observed fluxes or magnitudes with unity while retaining the

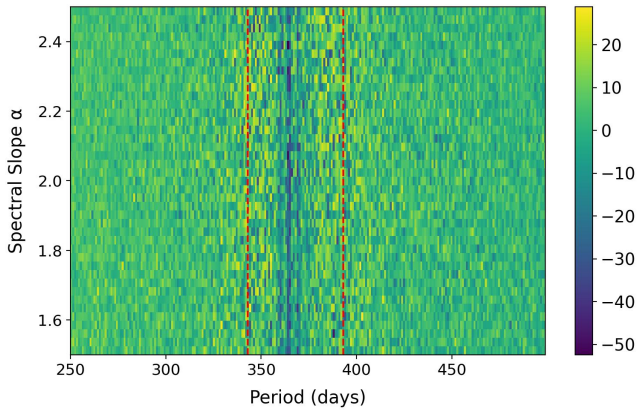

Figure A1. The figure shows a plot of the percentage power change after interpolation, with respect to the QPO periods and the spectral slopes of the simulated LCs. The red dashed line represents the 1σ exclusion region.

[48] https://www.oato.inaf.it/blazars/webt/

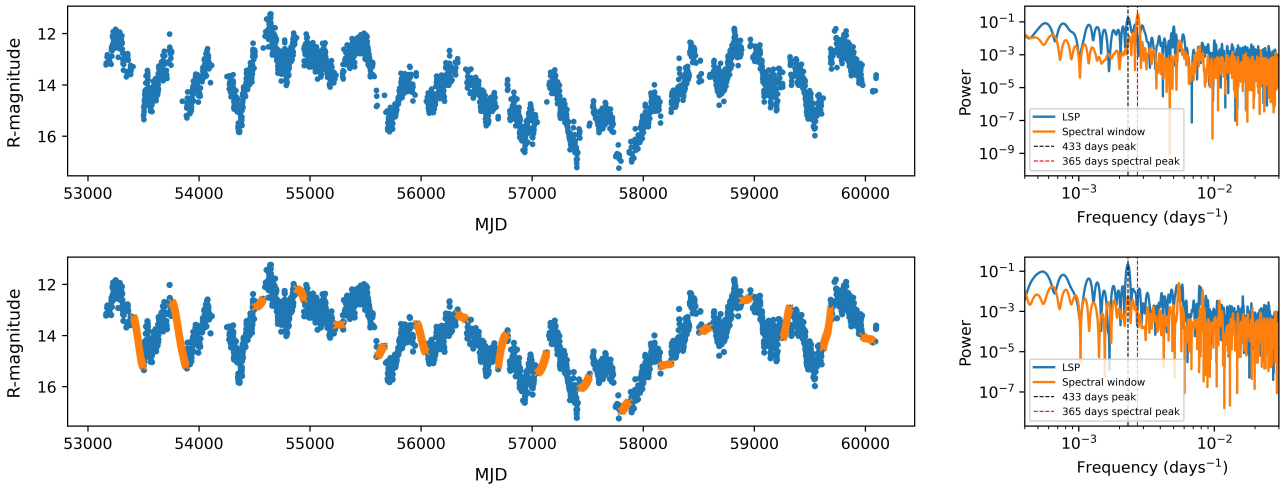

Figure A2. Top left: this figure displays an example of one of the simulated LCs with same time stamps as the original LC for $\alpha = 1.50$ having a QPO of 433 days. Top right: this plot shows an LSP of the simulated LC (in blue) and its spectral window response (in orange). Bottom left: similar to the top left but with interpolated gaps shown in orange. Bottom right: similar to the top right, but for the LC at the bottom left, showing improvement in peak signal after interpolation.

original observation times. The spectral window for our data (Figure 2) exhibits a peak near 365 days, as expected from annual observing gaps. Because this feature lies at 1 yr, any candidate periodicity on comparable timescales, such as the ∼433 day signal, requires careful scrutiny to distinguish genuine variability from sampling artifacts.

To investigate this issue, we performed forward simulations designed to reproduce both the intrinsic variability and the sampling properties of the data. We will start with simulations for a sample case and then generalize the results to a broader category (see Figure A1). We first generated a synthetic LC (LC_1) with 1 day sampling using the EMP 13 method, assuming a red-noise PSD with spectral index $\alpha = 1.50$. A QPO with a characteristic period of ∼433 days was then added in the time domain as a weakly modulated sinusoidal component, leaving the underlying red-noise PSD unchanged outside the narrow frequency range of the QPO. The simulated LC was subsequently resampled at the original observation times to produce LC_2, thereby imposing the same seasonal gaps and spectral window as the real data. The resulting LC_2 and its spectral window are shown in the top-left and top-right panels of Figure A2, respectively, with the latter matching that of the observed LC.

To test the robustness of the detected periodicity, we applied an additional diagnostic based on gap interpolation. Specifically, we interpolated LC_2 across the seasonal gaps using a piecewise cubic Hermite interpolating polynomial. This interpolation scheme was chosen because it preserves local monotonicity and avoids the overshooting commonly introduced by higher-order spline methods. Importantly, interpolation is not used here to recover or enhance the signal, but rather as a diagnostic perturbation of the sampling window: if a periodogram peak is substantially influenced by the window function, modest modifications to the gaps should lead to a substantial change in its power. Conversely, a genuine QPO is expected to remain comparatively stable. LC_2 and interpolated LC_2, along with their respective periodograms, are shown in Figure A2. We find that, for both the observed LC (Figure 2) and the simulated LC_2 (Figure A2), the power of the ∼433 day peak changes by no more than ∼10% after interpolation, corresponding to a global significance change of <5% for the observed LC.

To assess the generality of our results, we repeated the simulations across a range of spectral indices ($\alpha = 1.50$ to 2.50) and injected QPO periods between 250 and 500 days. The resulting percentage change in the power after interpolation is shown in Figure A1. We find that the power variation can reach around 50%, but these large changes are concentrated around 368 days. This effect occurs because the peak of the sampling window function coincides with this period. To quantify this effect more conservatively, we fitted a Gaussian function to the median power-change values (over each spectral index). From this fit, we derived a 1σ period range of 368 ± 23 days, indicated by the red dashed lines in Figure A1. Periods falling within this interval should therefore be treated carefully when claiming a QPO detection in LCs with yearly seasonal gaps. Based on this analysis, we excluded the 1σ region from our calculations and found that >98% of the periods have a power change of less than 15% for all spectral indices. Importantly, our detected QPO lies outside this affected range, placing it in a comparatively safe region of the period space. Finally, we estimated the corresponding change in global significance for the maximum-power variation across all simulations, which amounts to ∼17%. While this is not the universal threshold for an acceptable change in significance after interpolation, these results suggest that genuine QPOs are less sensitive to moderate perturbations of the sampling window, whereas window-induced features are expected to vary significantly more (P. Peñil et al. 2025). The relatively small changes in the power and significance of the 433 day peak, observed both in the real data and in simulated LCs containing an injected QPO, therefore suggest that this feature is unlikely to be a by-product of the annual observing gaps. This conclusion is further supported by a recent work (P. Peñil et al. 2025), which demonstrates that even extreme data loss with up to 70% missing observations does not suppress the detection significance of a periodic signal in LSP analyses. Taken together, the combined use of the spectral window, targeted simulations, and gap-interpolation diagnostics provides a robust framework for distinguishing true year-scale QPOs, such as the ∼433 day signal identified in the present study, from sampling artifacts.

ORCID iDs

Karan Dogra https://orcid.org/0009-0007-3214-602X
Alok C. Gupta https://orcid.org/0000-0002-9331-4388
C. M. Raiteri https://orcid.org/0000-0003-1784-2784
M. Villata https://orcid.org/0000-0003-1743-6946
Paul J. Wiita https://orcid.org/0000-0002-1029-3746
Mauri J. Valtonen https://orcid.org/0000-0001-8580-8874
S. O. Kurtanidze https://orcid.org/0000-0002-0319-5873
S. G. Jorstad https://orcid.org/0000-0001-6158-1708
R. Bachev https://orcid.org/0000-0002-0766-864X
G. Damljanovic https://orcid.org/0000-0002-6710-6868
C. Lorey https://orcid.org/0009-0002-5220-2993
S. S. Savchenko https://orcid.org/0000-0003-4147-3851
O. Vince https://orcid.org/0009-0008-5761-3701
J. A. Acosta-Pulido https://orcid.org/0000-0002-0433-9656
I. Agudo https://orcid.org/0000-0002-3777-6182
G. Andreuzzi https://orcid.org/0000-0001-5125-6397
D. A. Blinov https://orcid.org/0000-0003-0611-5784
G Bonnoli https://orcid.org/0000-0003-2464-9077
G. A. Borman https://orcid.org/0000-0002-7262-6710
M. I. Carnerero https://orcid.org/0000-0001-5843-5515
D. Carosati https://orcid.org/0000-0001-5252-1068
V. Casanova https://orcid.org/0000-0003-2036-8999
W. P. Chen https://orcid.org/0000-0003-0262-272X
Lang Cui https://orcid.org/0000-0003-0721-5509
P. U. Devanand https://orcid.org/0000-0003-3337-4861
E. G. Elhosseiny https://orcid.org/0000-0002-9751-8089
D. Elsaesser https://orcid.org/0000-0001-6796-3205
J. Escudero https://orcid.org/0000-0002-4131-655X
J. H. Fan https://orcid.org/0000-0002-5929-0968
K. Gazeas https://orcid.org/0000-0002-8855-3923
Minfeng Gu https://orcid.org/0000-0002-4455-6946
R. Z. Ivanidze https://orcid.org/0009-0005-7297-8985
M. D. Jovanovic https://orcid.org/0000-0003-4298-3247
G. N. Kimeridze https://orcid.org/0000-0002-5684-2114
Shubham Kishore https://orcid.org/0000-0001-8716-9412
E. N. Kopatskaya https://orcid.org/0000-0001-9518-337X
O. M. Kurtanidze https://orcid.org/0000-0001-5385-0576
V. M. Larionov https://orcid.org/0000-0002-4640-4356
Elena G. Larionova https://orcid.org/0000-0002-2471-6500
A. Marchini https://orcid.org/0000-0003-3779-6762
C. Marinelli https://orcid.org/0000-0002-3596-4307
A. P. Marscher https://orcid.org/0000-0001-7396-3332
D. Morcuende https://orcid.org/0000-0001-9400-0922
M. G. Nikolashvili https://orcid.org/0000-0003-0408-7177
J. Otero-Santos https://orcid.org/0000-0002-4241-5875
E. Semkov https://orcid.org/0000-0002-1839-3936
L. A. Sigua https://orcid.org/0000-0002-6985-2143
A. K. Singh https://orcid.org/0000-0001-7881-7748
M. Stojanovic https://orcid.org/0000-0002-4105-7113
A. Takey https://orcid.org/0000-0003-1423-5516
Amira A. Tawfeek https://orcid.org/0000-0002-8279-9236
Tushar Tripathi https://orcid.org/0009-0006-3586-2489
An-Li Tsai https://orcid.org/0000-0002-3211-4219
A. A. Vasilyev https://orcid.org/0000-0002-8293-0214
K. Vrontaki https://orcid.org/0009-0002-7669-7425
Zhongli Zhang https://orcid.org/0000-0002-8366-3373
Wenwen Zuo https://orcid.org/0000-0002-4521-6281

References

Abdi, H., et al. 2007, Encyclopedia of Measurement and Statistics, 3 (Sage)
Abdo, A. A., Ackermann, M., Ajello, M., et al. 2009, ApJ, 699, 817
Abdo, A. A., Ackermann, M., Ajello, M., et al. 2010, ApJ, 722, 520
Ackermann, M., Ajello, M., Albert, A., et al. 2015, ApJL, 813, L41
Ackermann, M., Ajello, M., Baldini, L., et al. 2010, ApJ, 721, 1383
Alston, W. N., Markeviciute, J., Kara, E., Fabian, A. C., & Middleton, M. 2014, MNRAS, 445, L16
Alston, W. N., Parker, M. L., Markevičiūtė, J., et al. 2015, MNRAS, 449, 467
Astropy Collaboration, Price-Whelan, A. M., Lim, P. L., et al. 2022, ApJ, 935, 167
Bhatta, G. 2017, ApJ, 847, 7
Bhatta, G. 2019, MNRAS, 487, 3990
Bhatta, G., & Dhital, N. 2020, ApJ, 891, 120
Bonning, E. W., Bailyn, C., Urry, C. M., et al. 2009, ApJL, 697, L81
Bonnoli, G., Ghisellini, G., Foschini, L., Tavecchio, F., & Ghirlanda, G. 2011, MNRAS, 410, 368
Caproni, A., Abraham, Z., & Monteiro, H. 2013, MNRAS, 428, 280
Conway, J. E., & Murphy, D. W. 1993, ApJ, 411, 89
Czesla, S., Schröter, S., Schneider, C. P., et al. 2019, PyA: Python astronomy-related packages, Astrophysics Source Code Library, ascl:1906.010
Dey, L., Valtonen, M. J., Gopakumar, A., et al. 2018, ApJ, 866, 11
Dogra, K., Gupta, A. C., Raiteri, C. M., et al. 2025, ApJS, 276, 1
Emmanoulopoulos, D., McHardy, I. M., & Papadakis, I. E. 2013, MNRAS, 433, 907
Fan, J. H., Kurtanidze, S. O., Liu, Y., et al. 2021, ApJS, 253, 10
Foreman-Mackey, D., Hogg, D. W., Lang, D., & Goodman, J. 2013, PASP, 125, 306
Foster, G. 1996, AJ, 112, 1709
Fuhrmann, L., Cucchiara, A., Marchili, N., et al. 2006, A&A, 445, L1
Gazeas, K. 2016, RMxAC, 48, 22
Gazeas, K. 2019, Galax, 7, 58
Gierliński, M., Middleton, M., Ward, M., & Done, C. 2008, Natur, 455, 369
Giommi, P., Blustin, A. J., Capalbi, M., et al. 2006, A&A, 456, 911
Gupta, A. C., Kushwaha, P., Valtonen, M. J., et al. 2023, ApJL, 957, L11
Gupta, A. C., Mangalam, A., Wiita, P. J., et al. 2017, MNRAS, 472, 788
Gupta, A. C., Srivastava, A. K., & Wiita, P. J. 2009, ApJ, 690, 216
Gupta, A. C., Tripathi, A., Wiita, P. J., et al. 2018, A&A, 616, L6
Gupta, A. C., Tripathi, A., Wiita, P. J., et al. 2019, MNRAS, 484, 5785
Hewitt, A., & Burbidge, G. 1989, ApJS, 69, 1
Holgado, A. M., Sesana, A., Sandrinelli, A., et al. 2018, MNRAS, 481, L74
Hughes, P. A., Aller, H. D., & Aller, M. F. 1985, ApJ, 298, 301
Jorstad, S. G., Marscher, A. P., Larionov, V. M., et al. 2010, ApJ, 715, 362
Jorstad, S. G., Marscher, A. P., Raiteri, C. M., et al. 2022, Natur, 609, 265
Kiehlmann, S. 2023, lcsim: LC simulation code, Astrophysics Source Code Library, ascl:2310.002
Kiehlmann, S., de la Parra, P. V., Sullivan, A. G., et al. 2025, ApJ, 985, 59
Kiehlmann, S., Max-Moerbeck, W., & King, O. 2023, wwz: Weighted wavelet z-transform code, Astrophysics Source Code Library, ascl:2310.003
King, O. G., Hovatta, T., Max-Moerbeck, W., et al. 2013, MNRAS, 436, L114
Kishore, S., Gupta, A. C., & Wiita, P. J. 2023, ApJ, 943, 53
Lachowicz, P., Gupta, A. C., Gaur, H., & Wiita, P. J. 2009, A&A, 506, L17
Lehto, H. J., & Valtonen, M. J. 1996, ApJ, 460, 207
Liska, M., Hesp, C., Tchekhovskoy, A., et al. 2018, MNRAS, 474, L81
Liu, Y., Jiang, D. R., & Gu, M. F. 2006, ApJ, 637, 669
Lomb, N. R. 1976, Ap&SS, 39, 447
Marscher, A. P., Gear, W. K., & Travis, J. P. 1992, in Variability of Blazars, ed. E. Valtaoja & M. Valtonen, 85 (Cambridge Univ. Press)
Marscher, A. P., Jorstad, S. G., D'Arcangelo, F. D., et al. 2008, Natur, 452, 966
Mashhoon, B., Hehl, F. W., & Theiss, D. S. 1984, GReGr, 16, 711
McHardy, I. M., Papadakis, I. E., Uttley, P., Page, M. J., & Mason, K. O. 2004, MNRAS, 348, 783
Mohan, P., Agarwal, A., Mangalam, A., et al. 2015, MNRAS, 452, 2004
Nalewajko, K., Gupta, A. C., Liao, M., et al. 2019, A&A, 631, A4
O'Neill, S., Kiehlmann, S., Readhead, A. C. S., et al. 2022, ApJL, 926, L35
Otero-Santos, J., Raiteri, C. M., Acosta-Pulido, J. A., et al. 2024, A&A, 686, A228
Pan, H.-W., Yuan, W., Yao, S., et al. 2016, ApJL, 819, L19
Peñil, P., Domínguez, A., Buson, S., et al. 2020, ApJ, 896, 134
Peñil, P., Torres-Albà, N., Rico, A., et al. 2025, MNRAS, 544, 4665
Peters, P. C. 1964, PhD thesis, California Institute of Technology
Raiteri, C. M., Stamerra, A., Villata, M., et al. 2015, MNRAS, 454, 353
Raiteri, C. M., Villata, M., Larionov, V. M., et al. 2007, A&A, 473, 819

Raiteri, C. M., Villata, M., Larionov, V. M., et al. 2008, A&A, 491, 755
Remillard, R. A., & McClintock, J. E. 2006, ARA&A, 44, 49
Rieger, F. M. 2004, ApJL, 615, L5
Romero, G. E., Chajet, L., Abraham, Z., & Fan, J. H. 2000, A&A, 360, 57
Roy, A., Chitnis, V. R., Gupta, A. C., et al. 2022b, MNRAS, 513, 5238
Roy, A., Sarkar, A., Chatterjee, A., et al. 2022a, MNRAS, 510, 3641
Sandrinelli, A., Covino, S., Dotti, M., & Treves, A. 2016, AJ, 151, 54
Sandrinelli, A., Covino, S., Treves, A., et al. 2018, A&A, 615, A118
Sarkar, A., Chitnis, V. R., Gupta, A. C., et al. 2019, ApJ, 887, 185
Sarkar, A., Gupta, A. C., Chitnis, V. R., & Wiita, P. J. 2021, MNRAS, 501, 50
Sarkar, A., Kushwaha, P., Gupta, A. C., Chitnis, V. R., & Wiita, P. J. 2020, A&A, 642, A129
Sasada, M., Uemura, M., Fukazawa, Y., et al. 2014, ApJ, 784, 141
Sbarrato, T., Ghisellini, G., Maraschi, L., & Colpi, M. 2012, MNRAS, 421, 1764
Scargle, J. D. 1982, ApJ, 263, 835
Smith, P. S., Elston, R., Berriman, G., Allen, R. G., & Balonek, T. J. 1988, ApJL, 326, L39
Stella, L., & Vietri, M. 1998, ApJL, 492, L59
Stellingwerf, R. F. 1978, ApJ, 224, 953
Timmer, J., & König, M. 1995, A&A, 300, 707
Tripathi, A., Gupta, A. C., Aller, M. F., et al. 2021, MNRAS, 501, 5997
Tripathi, A., Gupta, A. C., Smith, K. L., et al. 2024b, ApJ, 977, 166
Tripathi, A., Smith, K. L., Wiita, P. J., & Wagoner, R. V. 2024a, MNRAS, 527, 9132
Urry, C. M., & Padovani, P. 1995, PASP, 107, 803
Valtonen, M., Kidger, M., Lehto, H., & Poyner, G. 2008, A&A, 477, 407
Valtonen, M. J. 2024, RNAAS, 8, 276
Valtonen, M. J., Zola, S., Gupta, A. C., et al. 2024, ApJL, 968, L17
VanderPlas, J. T. 2018, ApJS, 236, 16
Vaughan, S., Uttley, P., Markowitz, A. G., et al. 2016, MNRAS, 461, 3145
Vercellone, S., D'Ammando, F., Vittorini, V., et al. 2010, ApJ, 712, 405
Villata, M., Raiteri, C. M., Aller, M. F., et al. 2007, A&A, 464, L5
Villata, M., Raiteri, C. M., Balonek, T. J., et al. 2006, A&A, 453, 817
Villata, M., Raiteri, C. M., Gurwell, M. A., et al. 2009, A&A, 504, L9
Villata, M., Raiteri, C. M., Sillanpaa, A., & Takalo, L. O. 1998, MNRAS, 293, L13
Villforth, C., Nilsson, K., Heidt, J., et al. 2010, MNRAS, 402, 2087
Wang, G. G., Cai, J. T., & Fan, J. H. 2022, ApJ, 929, 130
Wiita, P. J. 2011, JApA, 32, 147
Woo, J.-H., & Urry, C. M. 2002, ApJ, 579, 530
Zhou, J., Wang, Z., Chen, L., et al. 2018, NatCo, 9, 4599